Effects of Activated Ceria and Zirconia Nanoparticles on the Protective Behaviour of Silane Coatings in Chloride Solutions

Roohangiz Zandi Zand[1], Victoria Flexer[1], Michel De Keersmaecker[1], Kim Verbeken[2], Annemie Adriaens[1,*]

[1]Department of Analytical Chemistry, Ghent University, Krijgslaan 281-S12, B-9000, Ghent, Belgium
[2]Department of Materials Science and Engineering, Ghent University, Technologiepark 903, B-9052 Zwijnaarde (Ghent), Belgium
[*]E-mail: annemie.adriaens@ugent.be

This work investigates the effect of CeO_2 and ZrO_2 nanoparticles on the corrosion protection performance of non-inhibited and cerium inhibited silane coatings in 3.5% and 5% NaCl solutions on electro-galvanized steel substrates. Atomic force microscopy (AFM) results show relatively uniform coating thickness and varying nanoparticle distribution depending on coating composition. The corrosion behaviour of the sol–gel coatings revealed that CeO_2-ZrO_2 nanoparticles reinforce the barrier properties of the silane films and seem to act as nano-reservoirs providing a prolonged release of cerium ions. This prolonged release of inhibitor from oxide nanoreservoirs confers longer protection to the metallic substrate.

1. INTRODUCTION

Zinc is widely used as a protective coating to prevent corrosion of steel. Zinc is more electronegative than iron, and therefore offers anodic sacrifice protection to steel in corrosive media. For industrial zinc-coated substrates, it is important to delay or avoid "white rust" formation in humid environments, and consequently it is necessary to search for alternative methods for corrosion protection of galvanized steel [1-3]. Recently, hybrid silica-based sol-gel coatings attracted considerable interest, as they provide the formation of a thin organic coating that confers surface functionalization [4-6]. These coatings combine flexibility and good compatibility with paintings due to the organic component, and good mechanical properties and adhesion to the metallic substrate

conferred by the inorganic compound [7]. Silanes create a dense, oxygen-rich coating that generates a protective physical barrier [8]. However, these coatings are inert, and do not provide any active protection if aggressive species reach the metallic surface and initiate corrosion [6, 9]. Indeed, silane coatings present small pores, pinholes or micro cracks that facilitate electrolyte diffusion and the accumulation of aggressive species at the coating/substrate interface [10]. Therefore, the challenge is to modify the bulk properties of silane coatings by adding "active" protective species that further improve the corrosion resistance of the layer, or introduce self-healing capabilities [11].

A successful approach to improve the corrosion protection of silane coatings is based on the addition of oxide nanoparticles. These provide improved oxidation, corrosion, erosion and wear resistance. Extensive research has been carried out to enhance the corrosion resistance of metallic substrates by using ZrO_2 [6, 7, 12, 13], CeO_2 [14-17], SiO_2 [11, 14, 18-21], Al_2O_3 [22], TiO_2 [23, 24], and other mixed oxides. The amount of cracks and pores in sol-gel films can be decreased by incorporation of oxide nanoparticles into the hybrid matrix [12]. CeO_2 and ZrO_2, are particularly interesting due to their high corrosion, mechanical abrasion and wear resistance [6]. Montemor *et al.* [11] and Zheludkevich *et al.* [12] reported the modification of silane-based hybrid films with CeO_2, ZrO_2 or CeO_2-ZrO_2 nanoparticles. Results demonstrated that CeO_2 nanoparticles are very effective fillers, leading to both improved barrier and corrosion protection properties of the silane coatings. ZrO_2 nanoparticles produce an important enhancement of the barrier properties, and could act as a reservoir for corrosion inhibitors, but are otherwise inert [6]. Unfortunately, these films can no longer offer adequate protection if the coating is damaged due to the lack of self-healing capabilities.

Conversely, incorporation of corrosion inhibitors into sol-gel films can enhance the protective ability of the coatings, suppressing the corrosion process in the defects or where the coating has been damaged [12]. Among the most effective protective species, rare-earth salts offer good corrosion inhibition properties in addition to environmental friendliness [25]. Cerium nitrate has been successfully tested for corrosion protection of galvanized steel substrates, either as a conversion film [26-28] or as a corrosion inhibitor through addition to the silane formulation [25, 29-31]. However, corrosion inhibitors that are directly introduced into the silane formulation have difficulties to provide long-term protection of metals. In order to heal corrosion spots, a slow release of inhibitor would be desirable [32, 33]. This shortcoming calls for the development of nano-reservoirs to isolate inhibitors and prevent its direct interaction with the sol-gel matrix. Moreover, nanoparticle activation with cerium ions could reduce nanoparticle agglomeration due to stabilization of the surface charge [11]. In this way, the nanoparticles fix the cerium ions on their surface, distributing the inhibitor molecules homogenously in the bulk of the film and producing a slow release when required [7, 12].

Despite extensive work on the study of the unique properties of either CeO_2 or ZrO_2 nanoparticles, very little has been reported using a combination of both in the field of protective pre-treatments. Montemor *et al.* [6] investigated the electrochemical behaviour of modified silane-based hybrid films with CeO_2-ZrO_2 nanoparticles on galvanized steel substrate in diluted NaCl solution (0.005 M). Results demonstrated that CeO_2-ZrO_2 nanoparticles play an active role in the corrosion protection performance when they are added as fillers to hybrid silane coatings. The work did not study the possibility of adding an active corrosion inhibitor such as cerium ions to enhance even further the anti-corrosion protection. Additionally, a long term evaluation of corrosion inhibition of

silane films modified with rare earth salts-oxide nanoparticles in aggressive media, including mechanisms to stress the coating or artificial damage to evaluate the self-healing properties, would fill an important gap in the field.

The objective of this work was to investigate the effect of ceria and zirconia nanoparticles on protective behaviour of uninhibited and cerium inhibited silane hybrid coatings in aggressive media (3.5% and 5% NaCl, as opposed to 0.005M NaCl for the uninhibited CeO_2-ZrO_2 coatings mentioned above [6]). The hybrid silane film was prepared by the controllable hydrolysis of 3-glycidoxypropyltrimethoxysilane (GPTMS). The cerium salt activated nanoparticles were added after the hydrolysis step. The morphological features of the coated substrates were evaluated using atomic force microscopy (AFM). The corrosion behaviour of the sol–gel coatings was investigated using neutral salt spray tests, potentiodynamic polarization tests, and electrochemical impedance spectroscopy (EIS). Results show that the activation of CeO_2-ZrO_2 nanoparticles with cerium nitrate strongly improve the barrier properties of the silane films in concentrated NaCl and present better protective performance when compared with non-activated CeO_2-ZrO_2 filled system or systems filled with activated CeO_2 or ZrO_2 nanoparticles.

2. EXPERIMENTAL

2.1. Sample preparation

Ceria and zirconia nanoparticles (10 wt % in water, particle size < 25 nm and < 100 nm respectively, Sigma Aldrich) were activated by ultrasonic dispersion in an aqueous solution of $Ce(NO_3)_3$ (Fluka). Four sets of aqueous solutions were prepared. Set D contained CeO_2 and ZrO_2 nanoparticles, and $Ce(NO_3)_3$, while sets A, B and C where prepared with only two of the components (see Table 1).

Table 1. Composition and thickness of the coatings

Set	Mole ratio (mol %)			Coating thickness (μm)
	$Ce(NO_3)_3$ /Si	ZrO_2 /Si	CeO_2 /Si	
A (SHC- ZrO_2 + $Ce(NO_3)_3$)	0.0375	0.0125	-	61 ± 10
B (SHC- CeO_2 + $Ce(NO_3)_3$)	0.0375	-	0.0125	62 ± 12
C (SHC- ZrO_2 - CeO_2)	-	0.0250	0.0250	67 ± 15
D (SHC- ZrO_2- CeO_2+ $Ce(NO_3)_3$)	0.0250	0.0125	0.0125	75 ± 13

The silane solution was prepared by adding 4.084 mL of 3–glycidoxypropyl-trimethoxy silane (GPTMS, Merck) to 0.5 mL aqueous HCl (pH = 2), and stirred in a sealed beaker at room temperature for 20 min at 240 RPM to hydrolyse and condense the silane precursors. Next, the aqueous dispersion of nanoparticles was added and stirred for 10 min. For all samples the total Ce+Zr/Si mole ratio was 0.05. In the next step, 2.111 g of bisphenol A (BPA, Merck) was added to the solution as a cross-

linking agent. The BPA was dissolved by mixing the solution for 80 min. To accelerate the condensation reaction, 0.0152 mL of 1–methylimidazol (MI, Merck) was added to the solution and stirred for 5 min. A clear, colourless, homogenous solution resulted [34, 35].

Electro-galvanized steel samples (Arcelor Mittal, Gent, Belgium) consisted of coupons (1.13 cm^2 area and 0.1 cm thickness, for the AFM and electrochemical tests), and plates (7 × 15 × 0.1 cm, and, for the salt spray tests). The zinc coating had a weight of 112 g/m^2, and a thickness of 8 µm. The galvanized steel specimens were degreased using an alkaline cleaner, washed with distilled water, dried in air, and immersed in the silane solution for 60 s. The coated specimens were dried at room temperature for 24 h, and subsequently submitted to a 25–130 °C curing process with a heating rate of 7.5 °C/min for 90 minutes, to initiate extensive cross-linking in the hybrid films [35].

2.2. Analytical methods

The coating thickness was measured by profilometry (Check line 3000 pro, Germany).

Atomic force microscopy images were obtained under ambient conditions using a multimode scanning probe microscope (Digital Instruments, USA) equipped with a Nanoscope IIIa controller. 5 and 1 µm scans were recorded in tapping mode, using a silicon cantilever (OTESPA, Veeco). Nanoscope software version 4.43r8 was used to analyse the surface roughness, after the recorded images were modified using an automated X–Y-plane fit. The root mean square (RMS) surface roughness of the topographic images was calculated from the whole 5 × 5 µm images.

The protective performance of the coated substrates was evaluated in a neutral salt spray test that followed the ASTM B117 [36] procedure, using a 5 % NaCl solution. Prior to exposure, the back and the edges of the plates were covered with adhesive tape. An artificial scratch that reached the substrate was made in the coating to examine possible delamination. Visual assessment of the macroscopic surfaces was carried out at various time intervals throughout the total exposure time (264 h).

Potentiodynamic polarization test and electrochemical impedance spectroscopy (EIS) measurements were carried out to monitor the protective performance of the silane-treated galvanized steel substrates in a 3.5% NaCl solution (0.60 M), using an Autolab PG-STAT20 potentiostat equipped with a frequency response analyser (FRA) module. A three-electrode configuration cell was used with a Ag/AgCl KCl$_{sat}$ electrode as reference (all potentials quoted in this manuscript are referred to this electrode), and a platinum mesh as counter electrode. All electrochemical measurements were carried out at room temperature.

Potentiodynamic measurements were performed within the range of −1500 to 0 mV, at a scan rate of 1 mV s^{-1}. These experiments were replicated three times.

The corrosion resistance of the coatings was analysed using EIS measurements performed at the open circuit potential (OCP), which was measured during 120 min. Data were collected over a distributed frequency range of 10^5 - 10^{-2} Hz with a sinusoidal AC perturbation signal with a peak-to-peak amplitude of 10 mV. Impedance fitting was performed using the Z-view software (Scribner

Associates Inc.). For each coating type, triplicate electrodes were prepared and each coupon was measured three times.
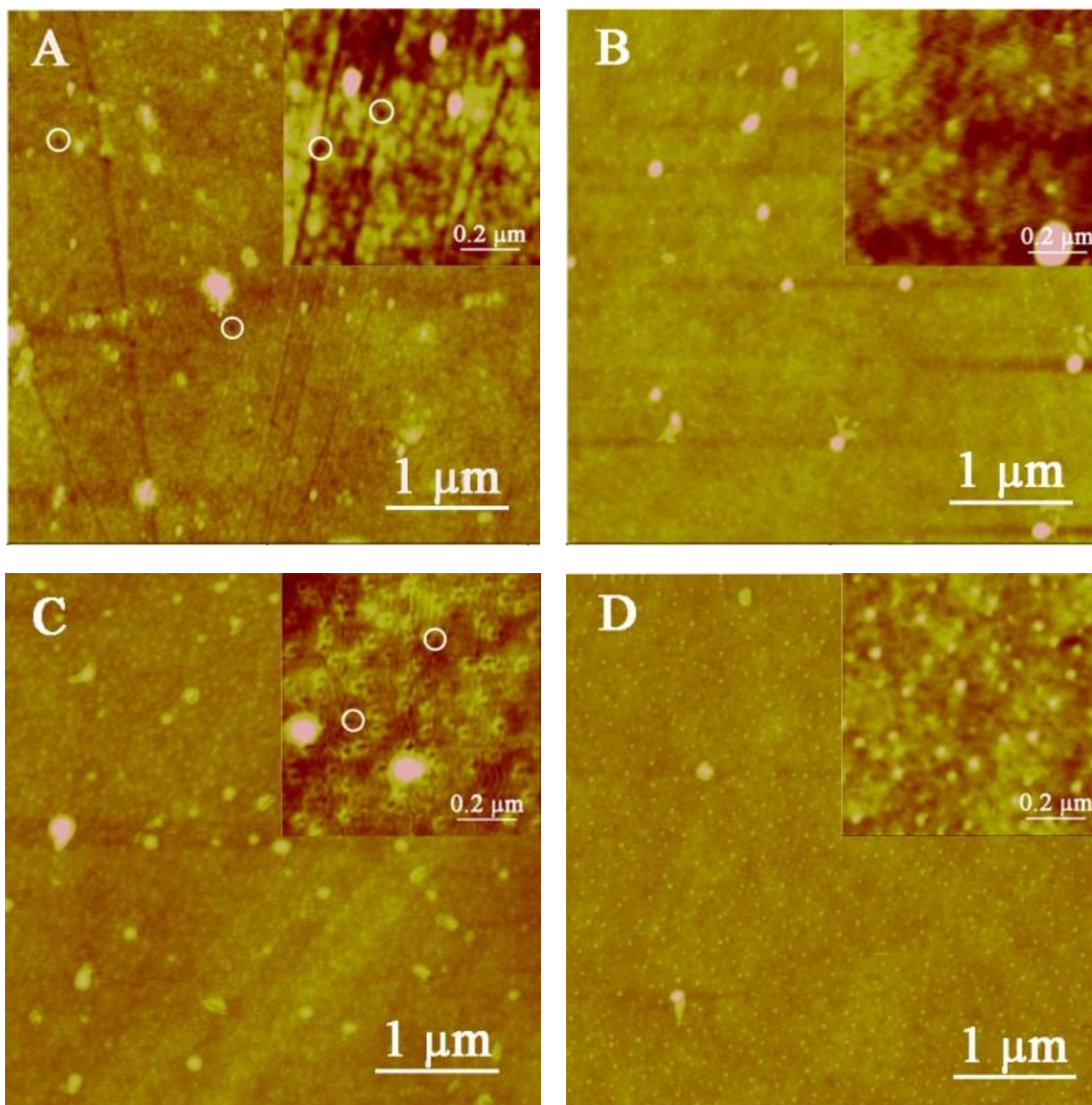
3. RESULTS

3.1. Surface morphology

Figure 1. AFM top-view images of hybrid silane films modified with CeO_2 and ZrO_2 nanoparticles: (A) $Ce(NO_3)_3 + ZrO_2$; (B) $Ce(NO_3)_3 + CeO_2$; (C) CeO_2-ZrO_2; (D) $Ce(NO_3)_3 + CeO_2$-ZrO_2. Pin holes in coatings A and C marked by white circles. Inset is a zoom image over the same scan area.

The coating thickness values are shown in Table 1. All films showed similar thickness values. The mean thickness values show a slight increase in going from coating A to D. However, the error in thickness measurements is in the same order as the thickness variation between different films (15-22%). Therefore, it is dubious to ascribe differences in protective behaviour to this variable.

The general surface morphology and the nanoparticle distribution in the different modified silane films can be observed in Figure 1. For coatings B and D, the surface morphology was very uniform with absence of defects or cracks. In coating D, the nanoparticles are about $20 - 50$ nm in diameter and uniformly distributed in the matrix when compared with the other samples (A, B, and C). Very few brighter spots (100-200 nm in diameter) are visible, which could either be ZrO_2 nanoparticles in the upper size limit (the manufacturer only informs the upper size limit, but no size distribution); or agglomerates of smaller nanoparticles on the surface [19, 30]. The size difference between the known dimensions of the added nanoparticles and the values measured by AFM can be explained by the presence of a silane layer on top of the nanoparticles. Thus, AFM measures the convexity of the surface caused by the underlying nanoparticles [6, 19]

For coating B, the AFM images show the presence of both agglomerates and small nanoparticles. The individual nanoparticles also appear to be 20 - 50 nm in diameter. In this case, the larger spots (100-300 nm) are readily classified as agglomerates, since this sample does not contain the larger ZrO_2 nanoparticles.

Coatings A and C show numerous nanoparticles aggregates. Moreover, these images reveal the presence of some nano-sized holes in the coatings, particularly for coating C. Two examples of these holes are highlighted in Figure 1C. The occurrence of coating defects is undesirable, since they may serve as initiators for pit corrosion through reduced coating thickness and/or as the initiation sites of fatigue cracks [37].

RMS surface roughness values of 0.722 nm, 0.955 nm, 0.855 nm, and 0.485 nm were measured for coatings A, B, C and D respectively. Differences in surface roughness arise from the presence of nanoparticles aggregates. Coating D distinctly shows the lowest surface roughness. Thus, AFM surface morphology demonstrates that the silane formulation D is the best for providing uniform morphology with low roughness, monodispersed nanoparticles, and absence of coating defects.

3.2. Salt spray tests

Salt spray tests were performed to qualitatively analyse the coating efficiency. Figure 2a and b present results of the exposure tests after 168 h and 264 h. An uncoated substrate, was tested as control. An artificial scratch was made to all coated samples to evaluate the protective efficiency of both the intact and damaged coatings.

After 168 h of exposure (Figure 2a) the uncoated substrate (Figure 2a,E) is heavily corroded with discoloration and pit formation. Samples A and C showed few spots of limited localized corrosion in the intact (non-damaged) coating, marked with black arrows in the images, which could be due to the presence of some pinholes in the coating layers as shown in AFM images (Figure 1A and C). In contrast, for coatings B and D no sign of corrosion was detected in the intact coating after 168 h.

The protective performance around the artificial scratch reveals the capacity of the coating to overcome coating damage. Sample (C) is heavily corroded in and around the edges of the scribe area (and particularly in the cross point), and shows a number of blisters together with white rust due to zinc coating degradation and formation of corrosion products such as zinc oxide and zinc hydroxide. The samples containing cerium nitrate (A, B and D) show lower delamination and corrosion products along the scribe area, as compared with sample C. The limited delamination in the presence of cerium nitrate suggests the availability of a corrosion inhibiting species.
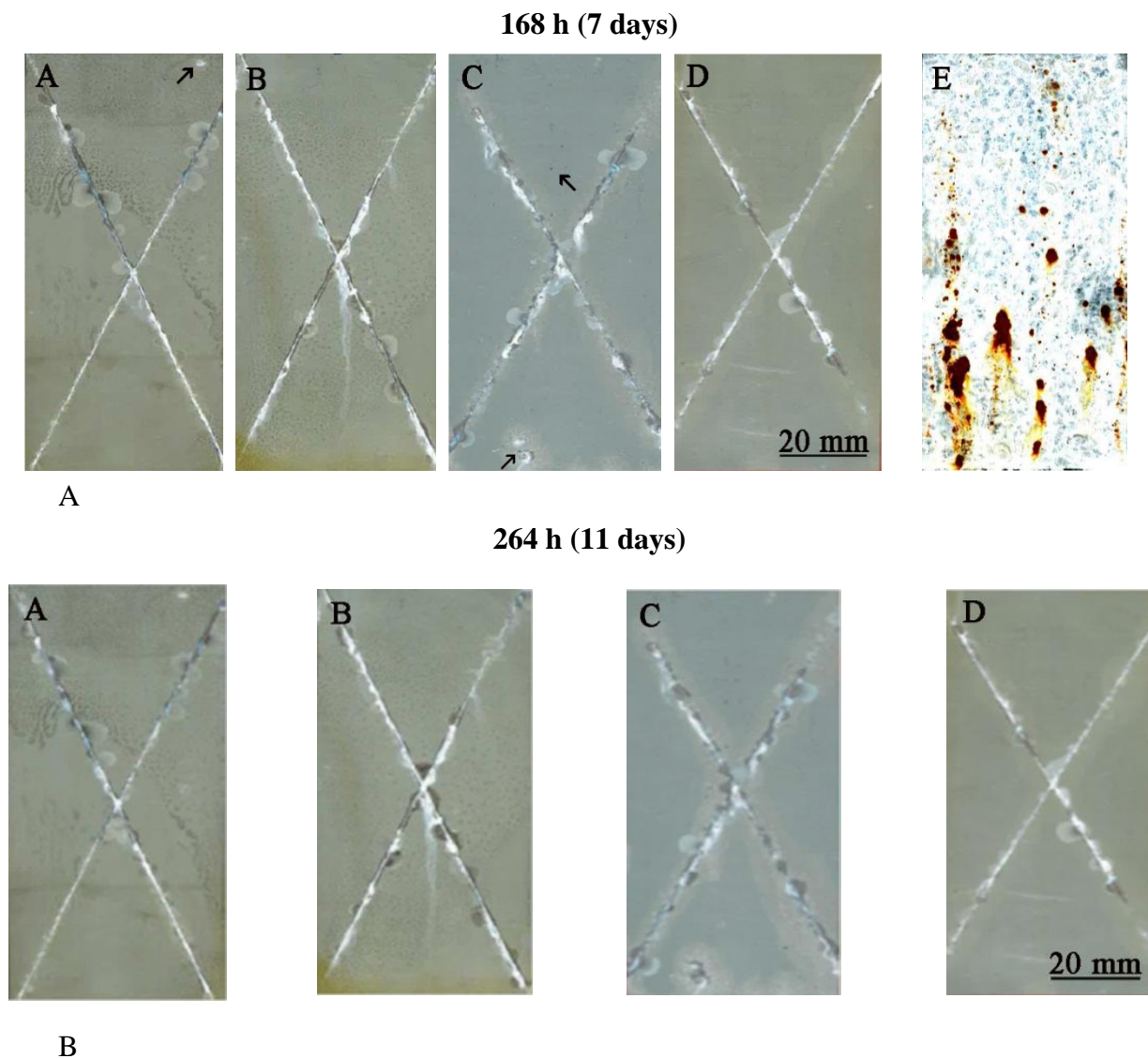
168 h (7 days)

A

264 h (11 days)

B

Figure 2. Photographs of uncoated and coated electro-galvanized steel samples with silane coatings A, B, C and D after 168 h (a) and 264 h (b) of salt spray exposure.

After 264 h of exposure (Figure 2b), no considerable changes were detected in the intact area in none of the coated samples, pointing towards the good barrier properties of the intact coatings. The few spots observed in samples A and C at 168h, remained the same size and aspect, suggesting self-healing capabilities to some extent for these coatings in the case of minor coating damage. In contrast,

around the scribe area, the breakdown of the coating layers in samples B and C progressed and this was followed by formation of red rust around the blisters, suggesting the presence of iron oxides, *i.e.* the bulk steel has already been corroded. The best performance was observed for samples A and D, *i.e.* the samples containing activated ZrO_2. A few blisters are observed, but blister growth rate seems to be considerably lower when compared with samples B and C. Samples A and D do not show formation of red rust in and around the scribed area. These coatings seem to be the most capable of overcoming the effects of coating damage.
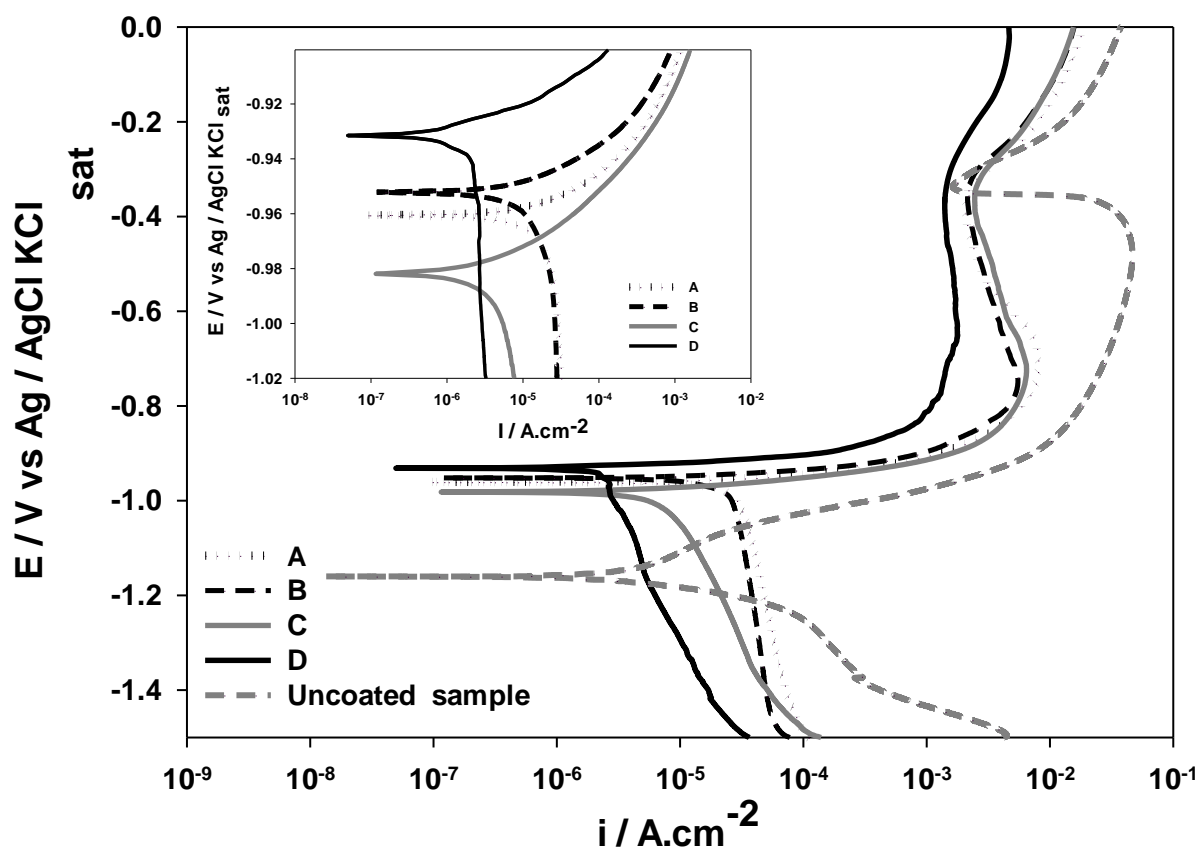
3.3. Potentiodynamic polarization

Figure 3. Potentiodynamic polarization curves for the uncoated and coated electro-galvanized steel samples with silane coatings A, B, C and D, obtained after 1 h of immersion in a 3.5 % NaCl solution. The inset shows a zoom around the corrosion potential of the coated samples.

Potentiodynamic polarization scans of coated and uncoated samples recorded after 1 h of immersion in 3.5% NaCl are presented in Figure 3. Both cathodic and anodic polarization curves were significantly shifted to lower current densities for all coated samples as compared to the uncoated sample. Moreover, the corrosion potentials of the coated samples showed a considerable shift in the noble direction. Because linearity is not achieved for a sufficiently large voltage interval, a quantitative Tafel analysis was not possible for any of the coated samples. The polarization curves still show

qualitatively the good barrier properties of all four coatings, with anodic currents at least one order of magnitude lower than the blank. All four coatings considerable decrease the available surface area for the corrosion reactions (oxygen reduction and metal dissolution), slowing down the corrosion activity, and hence the corrosion current density. These effects were more pronounced for coating D. Surprisingly, the initial slopes for the anodic branches of the coated samples are quite sharp, followed by a complete flattening of the current. This behaviour suggests that although the coatings are acting as a good barrier protecting most of the galvanized steel surface, the corrosion process is indeed very active in the few spots available for corrosion.

These results suggest that the enhanced corrosion protection of coating D is due to controllable release of cerium nitrate by nanoparticles (as reservoirs) in corroded spots, forming complexes with zinc charged species and reinforcing their protective role. These more stable corrosion products decrease even more the active area available for corrosion reactions.

3.4. Electrochemical impedance spectroscopy

The Bode plots obtained for the substrates pre-treated with different modified silane films during 244 h immersion in 3.5% NaCl solution are depicted in Figure 4. The Bode plots show that the impedance spectra are dependent on the nature of the dopant.
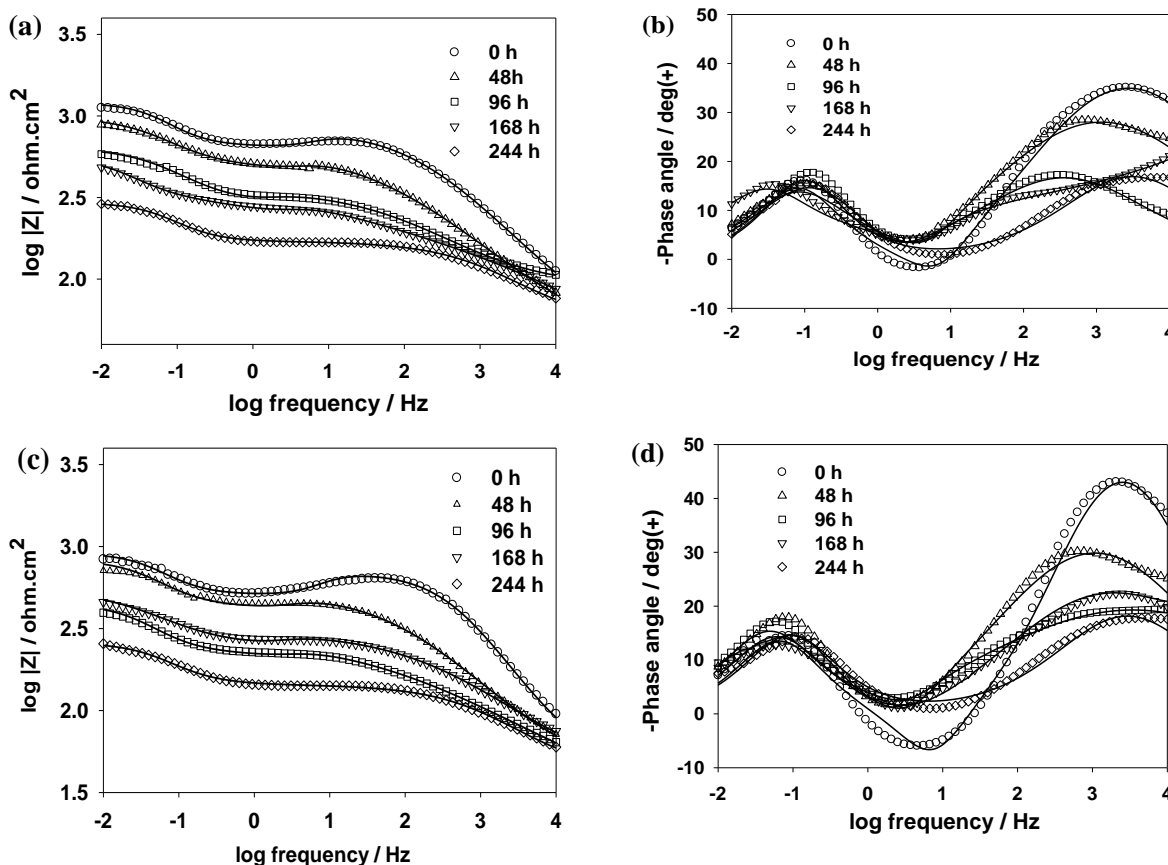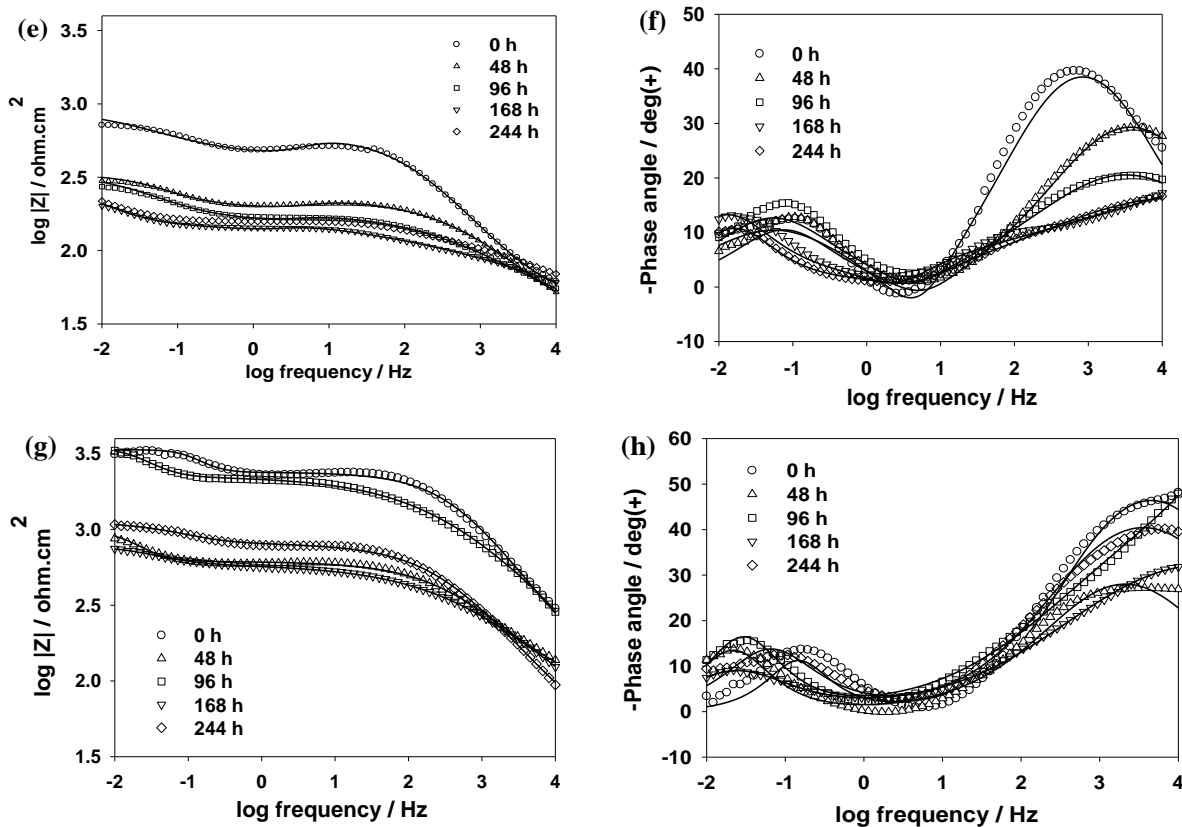
Figure 4. EIS Bode modulus (a, c, e, g) and phase angle (b, d, f, h) plots obtained for electro-galvanized steel samples pre-treated with silane coatings A (a, b), B (c, d), C (e, f), and D (g, h) during immersion in a 3.5 % NaCl solution. Solid lines show the fitted results to the equivalent circuits in Figure 5.

Sample D showed impedance magnitude values, that are almost 3 times higher than for the other samples at the initial stage of immersion (Figure 4g). After 48 h of immersion, the impedance of this sample decreases, which is most probably associated with water uptake. Water uptake could occur either around the few nanoparticle agglomerations, through nanopores of sizes below AFM resolution, or through pores formed at a later stage because of electrolyte exposure [38]. With further increase of immersion time, the impedance magnitude of sample D shows a considerable recovery, the EIS spectrum after 96 h shows very similar values to the original spectrum at the beginning of the immersion experiment. This recovery is attributed to the self-healing effect of cerium ions around the corrosion spots [10]. A new drop in impedance magnitude at 168 h is again followed by mild recovery at 244 h. Most important, after 244 h immersion, sample D still shows the highest impedance magnitude values at low frequencies of all four coatings. Such high impedance magnitude values confer higher corrosion protection of the silane films doped with $Ce(NO_3)_3$ and CeO_2-ZrO_2 nanoparticles.

Conversely, the impedance magnitude values for the other coatings (A, B and C) continuously decreased with time, except a small recovery for sample B after 168 h immersion (Figures 4 a, c and e). Sample C shows the lowest impedance magnitude values.

The shape of the phase angle plots, at the beginning of the immersion (0 h), indicated the presence of three time constants for coatings A, B and C (Figure 4b, d, f), consisting of a large capacitive loop at high frequencies which can be attributed to the capacitive behaviour of the silane film [39, 40]; an pseudo-inductive loop at medium frequencies, which may be related to the breakdown of the former protective surface film and corrosion activity due to adsorption of ions from the electrolyte solution (Cl$^-$ and Na$^+$) through the pores of the coating [41-46]; and followed by the second capacitive loop at low frequencies, which reveals corrosion activity and build-up of corrosion products [39, 40]. After a few hours of immersion, the EIS response starts to change and the phase angle plots evolved to two time constants consisting of two large capacitive loops at high and low frequencies. This change suggests that the coatings developed electrolyte conductive pathways through the pinholes and around the agglomerations (as shown in AFM images (Figure 1 A-C)), whereby the electrolyte could reach the substrate. The inductive loop has disappeared once the substrate has been fully adsorbed with ions. These ions will then start the corrosion process. For sample D, during immersion, the shape of the phase angle plots also indicated two capacitive loops at high and low frequencies. Interestingly, we do not observe the inductive loop here. This is probably too small because the pinholes are much smaller and there are almost no nanoparticles aggregates, which means less electrolyte penetrates, and the absorption of ions is much slower and hence not apparent in the phase plot.
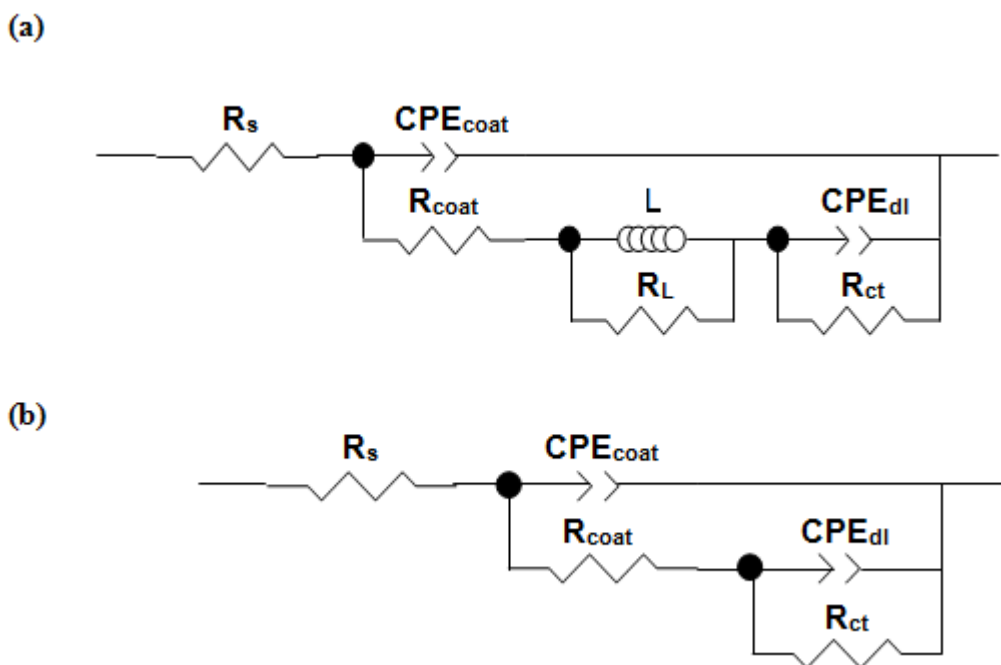

Figure 5. Equivalent circuits used for the numerical fitting of the EIS data during immersion in a 3.5 % NaCl solution.

A more detailed interpretation of the EIS results can be made by numerical fitting of the experimental data to the equivalent circuits depicted in Figure 5. Because the phase angle plots revealed two or three time constants at different immersion times, two different equivalent circuits were used to fit the data. The equivalent circuit shown in Figure 5a was used to model the EIS results of samples A, B and C at the beginning of immersion (0h). The equivalent circuit shown in Figure 5b

was used to model the EIS results of sample D during 244 h immersion, as well as samples A, B and C during 48 h to 244 h of immersion. The numerical simulations are plotted as full lines in Figure 4 a to h. These fittings are in very good agreement with the experimental data for all the samples.

Thus, for the equivalent circuits shown in Figure 5, R_s is interpreted as the resistance of the electrolyte; CPE_{Coat} and R_{Coat} represent the capacitance and resistance of the hybrid coatings, respectively; L and R_L represent the inductance and inductance resistance due to the adsorption reaction, respectively; CPE_{dl} is the capacitance of the electrochemical double layer at the metal/coating interface; and R_{ct} is the charge transfer resistance of the metal. In these equivalent circuits, constant phase elements (CPE) were used instead of pure capacitors, because of the non-ideal character of the corresponding response. This is due to presence of nanoparticles which give rise to a certain surface roughness and inhomogeneities. The true capacitances can be calculated from the respective CPE parameters, as described elsewhere [34]. The inductor which arises from adsorption effects could be defined as $L = R_L \tau$, where τ is the relaxation time for adsorption on the electrode surface [44]. The variation of the fitted parameters (resistances and capacitances) with immersion time using the equivalent circuits of Figure 5 are shown in Figure 6. Values are shown with the errors from the numerical fitting.
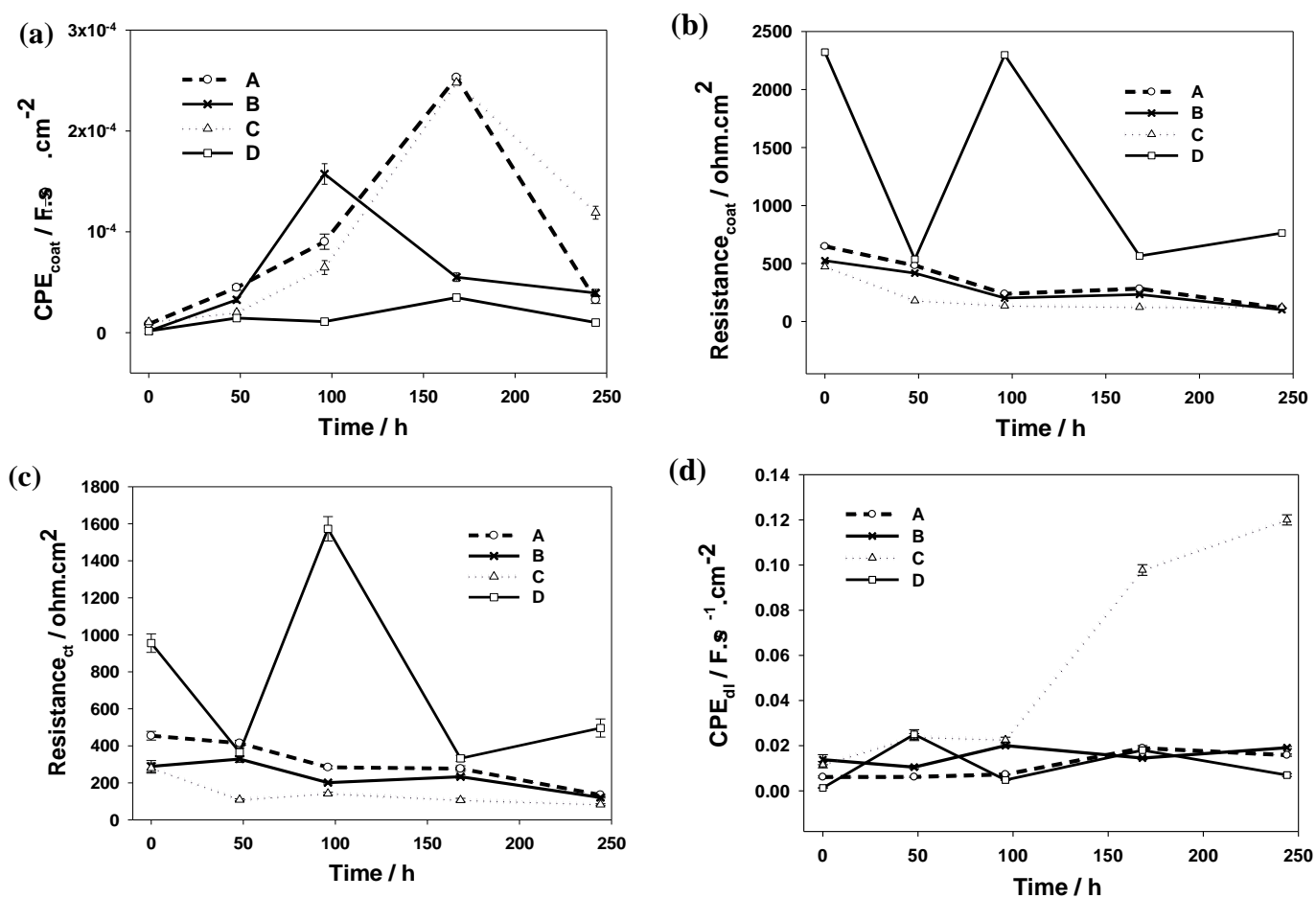

Figure 6. Evolution of the coating capacitance (a); coating resistance (b); charge transfer resistance (c); and double layer capacitance (d) during immersion in a 3.5 % NaCl solution.

The change of the silane hybrid film's capacitance (CPE_{coat}) during immersion is presented in Figure 6a. Generally the capacitance of dielectric films depends on the amount of absorbed water [12], thus increases in capacitance values are associated to water uptake [11]. Sample D has the lowest coating capacitance of the four systems examined over the whole immersion time. In addition, during immersion, the capacitance yields relatively constant values, with only a small increase after 168 h of immersion. This suggests a lesser amount of water uptake, because of the smaller nanopores (below AFM resolution), or nanopores only formed later, or the almost absence of nanoparticle agglomerations (as mentioned above). Sample B is also relatively stable; showing a small capacitance increase after around 96 h. The capacitance of samples A and C exhibit significantly faster growth during 168 h of immersion, as a result of more water uptake through the pores/defects present in the films [15]. The access of aggressive species induces localised corrosion activity. This is followed by precipitation of either insoluble corrosion products or the inhibition activity of the film, which block the pores/defects at the coating/substrate interface leading to a partial recovery of the coating barrier properties. This precipitation is translated in a decrease in coating capacitance after the increase due to water uptake. Decreasing coating capacitance is more pronounced for samples A and B, in comparison to sample C, probably because of the presence of cerium nitrate. These results suggest that the activation of nanoparticles with cerium ions had a beneficial impact on the coating capacitance and thus the protective behaviour.

The evolution of the coating resistance (R_{coat}) of the sol–gel layers, is shown in Figure 6b. Sample D has the highest coating resistance during the 244 h immersion period; however the resistance decreases both at 48 h and 168 h suggesting the formation of some pores or the enlargement of smaller pores in the sol–gel layer [38]. In both cases, the coating resistance recovers, which is attributed to the self-healing properties of this coating. The coating resistance of samples A, B and C is lower in comparison to coating D, particularly in the case of the coating C. The coating resistance values of these films show a gradual decrease during immersion because of their porous structures. Because these pores are larger than in the case of coating D, the self-healing capabilities are not enough and cannot compensate the damage. The coating resistance of sample D was always, even after 244 h exposure, at least twice as high as the other samples.

Figure 6c and d show the evolution of the charge transfer resistance (R_{ct}) and double layer capacitance (CPE_{dl}) values during immersion that are associated with the development of a time constant in the low-frequency range of the EIS spectra. For samples A, B and C, the low frequency resistance (R_{ct}) reveals lower values than for coating D and a small decrease during immersion (Figure 6c). In contrast, sample D shows some fluctuations, with a rapid drop and later recovery attributed to the self-healing properties. After 244 h of immersion, this coating shows a charge-transfer resistance, which is about 3 times higher than the other sol-gel films.

The CPE associated with the corrosion process (CPE_{dl}), remains almost constant for samples A and B over immersion for 244 h, reflecting the stability and the good barrier properties of the coating. In contrast, the CPE_{dl} values for sample C are higher and showed a pronounced increase because of the enlargement of the pores, appearance of cracks or even peeling of the coating. Indeed some coating peeling was evident to the naked eye for coating C at the end of the immersion period. For sample D, the low-frequency capacitance passes through small maxima after 48h and 168 h immersion, and then

starts to decrease. These values agree with the evolution of the low-frequency resistance of the film. The evolution of the low-frequency resistance shows an increase after 96 h immersion, accompanied by a decrease in the CPE, i.e. as expected, the CPE_{dl} changes in the opposite direction as R_{ct}. Since the corrosion activity occurred in localised areas because of water uptake, it is likely that the precipitation of the insoluble and passive self-healing products occurred at these locations, thereby decreasing the corrosion activity at the interface [15].

4. DISCUSSION

The electrochemical results are in good agreement with the AFM images and the salt-spray tests. There is a clear correlation between protective performance and surface morphology. Sample C, containing non-activated CeO_2-ZrO_2 nanoparticles, shows both a large number of nanoparticles aggregates as well as several cracks or pores. This sample was the least performing in all corrosion tests: faster corrosion, red rust formation and even some localised corrosion in the undamaged coating in the salt spray test, the lowest E_{corr}, and the impedance fitting parameters that showed the highest permeability to water, and hence aggressive species. Montemor *et al.* analysed this specific coating (CeO_2-ZrO_2 nanoparticles without cerium inhibitor) and found it was efficient and stable when exposed to diluted NaCl concentrations (0.005M) [6]. However, our results show that under more aggressive conditions, the nanoparticle reinforcing capabilities on the silane coating are not sufficient to protect the substrate.

While none of the analysed coatings remained unchanged under the extreme aggressive conditions applied, all experimental evidence shows that the combination of CeO_2 and ZrO_2 nanoparticles and cerium ions (coating D) outperforms the other coatings. The better performance in the corrosion tests strongly suggests that the addition of cerium ions to the CeO_2-ZrO_2 nanoparticles dispersion creates an important synergy, reinforcing the protection of the silane films [11]. The combination of two types of nanoparticles and the cerium ions doping produces the more homogeneous coating. The almost absence of nanoparticle aggregates could be due to less attraction between different nanoparticles (ZrO_2 and CeO_2), the repulsive effects of charged particles (in the presence of $Ce(NO_3)_3$), and the stabilization of the surface charge, as previously reported [12]. These effects are also present in coatings A and B, but not C. Indeed, a plausible explanation for the higher degree of nanoparticle aggregation and probably related extended nanoporosity of coating C could be the non-activation of the nanoparticles. Thus, besides the already reported corrosion inhibition and healing capabilities of $Ce(NO_3)_3$ [7, 12, 25-28, 31], our experimental evidence suggests that in combination with ZrO_2 and/or CeO_2 nanoparticles, it contributes to the reinforcement of the coating, by diminishing its porosity.

EIS responses indicate changes in the coating long time before any visible damage occurs (as observed for example by salt spray test). Thus, while the salt spray is an excellent indicator of healing capabilities around coating damaged areas, EIS evaluates apparent intact coatings. Even though no pores or cracks were observed for coatings B and D by AFM, EIS showed that when subject to stressing conditions, water uptake does occur, and hence some corrosion activity starts to develop

(though invisible to the naked eye at this point). The reported self-healing properties of cerium ions are most evident in the rather sharp changes in both coating and charge transfer resistance values for coating D. These changes are associated with recovery after an initial aggression.

Finally, performances shown by coatings A and B are quite similar. Coating A showed one spot of localised corrosion in an undamaged area and coating B did not. On the other hand, coating B showed some red rust around the damaged area after 264 h in salt spray, whereas coating A did not. Most probably the small spot of localised corrosion in A is associated with the small pores observed by AFM (not observed for B). Conversely, the absence of red rust for this same coating, suggests that the ZrO_2 nanoparticles are more effective as nano-structured Ce-ion reservoirs and can provide longer release of the inhibitor ions [15], than the CeO_2 nanoparticles.

Previous work has outlined possible mechanisms to explain the corrosion inhibition effects of silane films, rare earth salts and oxide nanoparticles. Water uptake through the pre-existent pinholes in the coating causes development of anodic and cathodic activity. Under the conditions tested in the present work, the main cathodic reaction is oxygen reduction with production of hydroxyl ions. The Zn^{2+} ions produced at the anodic areas migrate to the cathodic spots where they combine with OH^- to form zinc corrosion products, which in the presence of chloride ions also lead to the formation of simonkolleite and/or other zinc chloride charged ions as reported in the literature [6, 11]. Simultaneously to these processes, and under an increased pH, the Si-O-Si network starts to decompose into a hydrated and expanded gel [11, 15, 20]. In a first step there is formation of silicates, which may provide some protection in small defects or pores. It has been reported that a passive film composed of $Zn(OH)_2$ and $ZnSi_2O_5$ may form on the active areas and that preferential precipitation of zinc silicate occurred on the defects of the passive film, delaying the corrosion activity [15].

As the pH becomes more alkaline, the deterioration of the silica network starts to release the CeO_2 and/or ZrO_2 nanoparticles, which are, in contrast, very stable under alkaline pH [11, 15]. The CeO_2 nanoparticles have a very high affinity for oxygen and for charged ions, like Zn^{2+}, compensating defects in the oxygen sub–lattice. CeO_2 can co-precipitate together with the zinc corrosion products, leading to a more stable and protective surface layer, which polarizes the anodic reactions and inhibits the corrosion activity [11, 15, 20].

Additionally, cerium ions released from the nanoparticles may form highly insoluble $Ce(OH)_3$ which can be formed in the spots where the cathodic reaction occurs [47]. The oxidation of Ce^{3+} to Ce^{4+} by peroxide species produce precipitation of $Ce(OH)_4$. ZrO_2 nanoparticles have been reported to act as a reservoirs for corrosion inhibitors, but are otherwise inert [6].

Finally, as briefly explained, because of the relatively large error in the thickness measurements, it is dubious to make assertions about the effect of a possible minor increase in coating thickness on going from coating A to D. After having analysed all the experimental evidence, we believe that the observed differences in performance are most probably not explained by the possible differences in coating thickness. Indeed, while coating D could be up to 20% thicker than its counterparts, it shows low frequency impedance values more than three times higher than the other coatings. Moreover, while coating C shows the putatively second largest thickness value, it is clearly the least performing coating.

5. CONCLUSIONS

Hybrid silane coatings doped with four different combinations of CeO_2 and ZrO_2 nanoparticles and $Ce(NO_3)_3$ ions were synthetized and tested as protective protection for electro-galvanized steel substrates. All coatings showed very high protection as compared to an uncoated sample.

Morphology and corrosion studies reveal that the presence of cerium ions reduces the corrosion rate of the metal substrate. These results show that cerium ions in combination with CeO_2 and ZrO_2 nanoparticles, produce a better sealed coating, with almost no nanopores or cracks. Incorporation of activated CeO_2-ZrO_2 nanoparticles reduces the cathodic and anodic current density to lower values and shifts the voltage to more positive potentials.

EIS results revealed self-healing properties of the Ce ions that were most evident in the rather sharp changes in both coating and charge transfer resistance values for the coating containing activated CeO_2-ZrO_2 nanoparticles. The highest impedance magnitude value of this coating suggested that the CeO_2-ZrO_2 nanoparticles are more effective as nanostructured cerium ion reservoirs and can provide prolonged release of the inhibitor ions. The prolonged release of cerium ions from oxide nano-reservoirs confers longer protection of the metallic substrate. This coating can be a prospective candidate for the development of new environmentally friendly protective pre-treatments.

References

1. J.D. Yoo, K. Ogle and P. Volovitch, *Corros Sci*, 81, (2014), 11.
2. E. Diler, B. Lescop, S. Rioual, G. Nguyen Vien, D. Thierry and B. Rouvellou, *Corros Sci* 79, (2014), 83.
3. J. Duchoslav, R. Steinberger, M. Arndt and D. Stifter, *Corros Sci*, In Press, (2014).
4. S. Dalbin, G. Maurin, R.P. Nogueira, J. Persello and N. Pommier, *Surf Coat Tech* 194, (2005), 363.
5. *Directive number 2003/53/EC of the European Parliament and Council.*, 18 June 2003), L 178/24-L 178/27.
6. M.F. Montemor, W. Trabelsi, S.V. Lamaka, K.A. Yasakau, M.L. Zheludkevich, A.C. Bastos and M.G.S. Ferreira, *Electrochim Acta* 53, (2008), 5913.
7. M.L. Zheludkevich, R. Serra, M.F. Montemor and M.G.S. Ferreira, *Electrochem Commun*, 7, (2005), 836.
8. M. Wang, D. He, H. Xie, L. Fu, Y. Yu and Q. Zhang, *Thin Solid Films*, 520, (2012), 5610.
9. C. Motte, M. Poelman, A. Roobroeck, M. Fedel, F. Deflorian and M.G. Olivier, *Prog Org Coat*, 74, (2012), 326.
10. W. Trabelsi, P. Cecílio, M.G.S. Ferreira, K. Yasakau, M.L. Zheludkevich and M.F. Montemor, *Prog Org Coat*, 59, (2007), 214.
11. M.F. Montemor and M.G.S. Ferreira, *Electrochim Acta* 52, (2007), 6976.

12. M.L. Zheludkevich, R. Serra, M.F. Montemor, K.A. Yasakau, I.M.M. Salvado and M.G.S. Ferreira, *Electrochim Acta*, 51, (2005), 208.
13. A.R. Phani, Gammel, F. J., Hack, T. and Haefke, H, *Mater Corros* 56, (2005), 77.
14. F. Deflorian, M. Fedel, S. Rossi and P. Kamarchik, *Electrochim Acta* 56, (2011), 7833.
15. M.F. Montemor, R. Pinto and M.G.S. Ferreira, *Electrochim Acta* 54, (2009), 5179.
16. F. Brusciotti, A. Batan, I. De Graeve, M. Wenkin, M. Biessemans, R. Willem, F. Reniers, J.J. Pireaux, M. Piens, J.Vereecken and H. Terryn, *Surf Coat Tech* 205, (2010), 603.
17. M. Schem, T. Schmidt, J. Gerwann, M. Wittmar, M. Veith, G.E. Thompson, I.S. Molchan, T. Hashimoto, P. Skeldon, A.R. Phani, S. Santucci and M.L. Zheludkevich, *Corros Sci* 51, (2009), 2304.
18. B:P. Mosher, C. Wu, T. Sun and T. Zeng, *J Non-Cryst solids*, 352, (2006), 3295.
19. A. Phanasgaonkar and V.S. Raja, *Surf Coat Tech* 203, (2009), 2260.
20. M.F. Montemor and M.G.S. Ferreira, *Prog Org Coat*, 63, (2008), 330.
21. N.C. Rosero-Navarro, S.A. Pellice, A. Durán and M. Aparicio, *Corros Sci* 50, (2008), 1283.
22. H.M. Hawthorne, A. Neville, T. Troczynski, X. Hu, M. Thammachart, Y. Xie, J. Fu and Q. Yang, *Surf Coat Tech*, 176, (2004), 243.
23. S.W. Lamaka, M.L. Zheludkevich, K.A. Yasakau, R. Serra, S.K. Poznyak and M.G.S. Ferreira, *Prog Org Coat* 58, (2007), 127.
24. Q.W. Suning Li, Tao Chen, Zhihua Zhou, Ying Wang and Jiajun Fu, *Nanoscale res Lett*, 7, (2012), 227.
25. M.F. Montemor, W. Trabelsi, M. Zheludevich and M.G.S. Ferreira, *Prog Org Coat*, 57, (2006), 67.
26. K. Aramaki, *Corros Sci* 45, (2003), 1085.
27. K. Aramaki, *Corros Sci* 43, (2001), 1573.
28. K. Aramaki, *Corros Sci*, 46, (2004), 1565.
29. R.Z. Zand, K. Verbeken and A. Adriaens, *Int J Electrochem*, 8, (2013), 548.
30. R.Z. Zand, K. Verbeken and A. Adriaens, *Int J Electrochem*, 8, (2013), 4924.
31. A.M. Cabral, W. Trabelsi, R. Serra, M.F. Montemor, M.L. Zheludkevich and M.G.S. Ferreira, *Corros Sci* 48, (2006), 3740.
32. S. Zheng and J. Li, *J Sol-Gel Sci Techn*, 54, (2010), 174.
33. A.N. Khramov, N.N. Voevodin, V.N. Balbyshev and M.S. Donley, *Thin Solid Films*, 447–448, (2004), 549.
34. R. Zandi Zand, K. Verbeken and A. Adriaens, *Prog Org Coat*, 75, (2012), 463.
35. R. Zandi Zand, K. Verbeken and A. Adriaens, *Prog Org Coat*, 72, (2011), 709.
36. *ASTM B117-03 Standard Practice for Operating Salt Spray (Fog) Apparatus, Annual Book of ASTM Standards, 03.02, ASTM International, United States*, 2004),
37. N.N. Voevodin, V.N. Balbyshev and M.S. Donley, *Prog Org Coat*, 52, (2005), 28.
38. A. Pepe, M. Aparicio, A. Durán and S. Ceré, *J Sol-Gel Sci Techn* 39, (2006), 131.
39. W. Trabelsi, P. Cecilio, M.G.S. Ferreira and M.F. Montemor, *Prog org Coat*, 54, (2005), 276.
40. W. Trabelsi, E. Triki, L. Dhouibi, M.G.S. Ferreira, M.L. Zheludkevich and M.F. Montemor, *Surf Coat Tech*, 200, (2006), 4240.
41. P.D. Deck, M. Moon and R.J. Sujdak, *Prog Org Coat*, 34, (1997), 39.
42. A. Neville and C. Wang, *Wear*, 267, (2009), 195.
43. M.E.Orazem, B.Tribollet, *Electrochemical impedance spectroscopy, John Wiley & Sons, INC*, 2008),
44. S.A. Umoren, Y. Li and F.H. Wang, *J Solid State Electrochem*, 14, (2010), 2293.
45. Zomorodian, A., F. Brusciotti, A. Fernandes, M.J. Carmezim, T. Moura e Silva, J.C.S. Fernandes and M.F. Montemor, *Surf Coat Tech*, 206, (2012), 4368.
46. X. Liu, T. Romeo, J. Weber, T. Scheuermann, S. Moulton, G. Wallace *Acta Biomater*, 9, (2013), 8671.

47. K.A. Yasakau, M.L. Zheludkevich, O.V. Karavai and M.G.S. Ferreira, *Prog Org Coat*, 63, (2008), 352.